Photorefractive parametric scattering in the ferroelectric relaxor SBN: Phenomenological and application aspects

M. Goulkov and O. Fedorenko
Institute of Physics, Science Ave 46, 03650, Kiev-39, Ukraine

L. Ivleva
Institute of General Physics, Moscow, Russia

M. Böttcher, Th. Woike, and T. Granzow*
Institute of Mineralogy, University of Cologne, Germany

M. Imlau and M. Wöhlecke
Department of Physics, University of Osnabrück, Germany

(Received 26 April 2004; revised manuscript received 29 October 2004; published 14 January 2005)

This paper is dedicated to the study of a new class of light-induced parametric scattering recently found in photorefractive $Sr_{0.61}Ba_{0.39}Nb_2O_6:Cr$ (SBN:Cr). The scattering consists of polarization-isotropic cones induced by two pump beams and forming series of vertical lines on the observation screen. It is due to a type of 4WM processes between pump and scattering waves involving the fundamental grating recorded by the pump beams. A complete phenomenological analysis of the new 4WM model is presented. The scattering hysteresis under external fields and the temperature evolution of the new scattering are studied. It is shown that the parametric scattering is a useful tool for studying ferroelectric and relaxor properties of SBN.

DOI: 10.1103/PhysRevB.71.024104 PACS number(s): 78.20.Jq, 42.65.Hw, 42.70.Nq

I. INTRODUCTION

Propagation of laser beams in crystals with a high photorefractive nonlinearity often results in light-induced scattering. The particular interest in this effect has grown considerably during the last decades due to various fundamental and technological aspects. High amplification rates reported for photorefractive scattering encourage its use for different nonlinear optical applications like, e.g., amplification and transmission of weak optical signals and images,[1,2] mixing of mutually incoherent beams,[3] etc. Because of its photorefractive origin, light-induced scattering contains information about electric charge transport mechanisms and various material constants, and therefore is an effective tool for contactless characterization of materials.[4–7] Light-induced scattering is seeded by coherent optical noise originating from optical inhomogeneities of the crystal. These seed waves interfere with pump waves of the transmitted part of the incident light. They record a large variety of elementary refractive index gratings via the photorefractive effect.[8] Mutual diffraction of seed and pump waves on these noisy gratings results in an enhancement of the coherent noise, and light-induced scattering develops. Usual two-wave mixing processes[9] involve only one seed wave and one pump wave and result in wide-angle scattering (also called beam fanning). The angular distribution of the scattered light can be strongly asymmetric [one-lobe pattern in $Sr_xBa_{1-x}Nb_2O_6$ (SBN) and $BaTiO_3$[10,11]] or more or less symmetric (two-lobe pattern in doped $LiNbO_3$ and $LiTaO_3$[12]), depending on the particular type of photorefractive response of the crystal. A more complicated and impressive type of light-induced scattering is parametric scattering, which results in a rich variety of different ring and line patterns on a viewing screen behind the crystal.[13,14] This type is due to four-wave mixing (4WM) processes where two pump and two seed waves are involved. The spatial geometry of the scattering pattern is defined by the phase-matching conditions of the corresponding 4WM process, and the intensity of scattered light depends on the efficiency of the wave mixing.

The direct correlation between photorefractive and ferroelectric properties was shown by studying beam fanning in SBN.[15,16] Taking into account the direct dependence of the efficiency of the scattering processes on the state of the spontaneous polarization P_s, it was suggested[17] that a temperature study of light-induced scattering in photorefractive ferroelectrics is an especially promising tool for studying the evolution of the polar structure in the vicinity of the phase transition. A progress in the theoretical study of the processes of parametric amplification of scattered light is important for further development of a general 4WM theory. Developing a deeper understanding of parametric mixing of pump beams with coherent noise is a task not only for photorefractive ferroelectrics in particular, since parametric scattering is a general effect found in many optical materials with different types of nonlinearity.[18–21]

The first extended classification of parametric scattering by different 4WM processes proposed in Ref. 22 is based on the following phase-matching conditions:

$$\text{rings:} \quad \mathbf{k}_\alpha + \mathbf{k}_\beta = \mathbf{k}_\delta + \mathbf{k}_\gamma, \tag{1}$$

$$\text{lines:} \quad \mathbf{k}_\alpha - \mathbf{k}_\beta = \mathbf{k}_\delta - \mathbf{k}_\gamma. \tag{2}$$

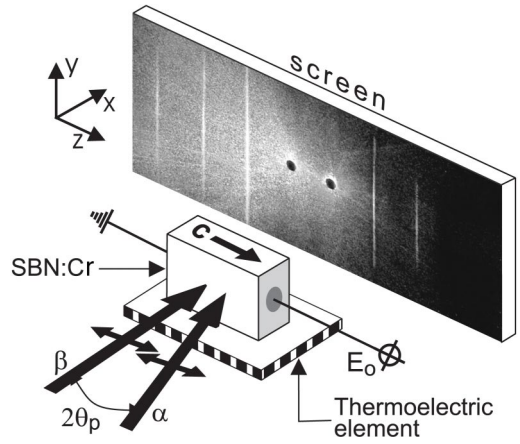

FIG. 1. Experimental setup and scattering patterns from two extraordinary pump beams α and $\beta(2\theta_p=5°)$ observed on a viewing screen. The SBN sample is placed on a stack of Peltier elements to control the crystal temperature. The crystal's *c* faces are connected to a dc power supply.

These conditions parametrically couple the wave vectors $\mathbf{k}$ of the pump waves α, β and the seed waves γ, δ via pairs of identical gratings recorded by combinations of different seed and pump waves: $\gamma-\beta$ and $\delta-\alpha$. At the same time, diffraction of the waves α and β on these gratings enhances the seed waves δ and γ. In the general case, waves in Eqs. (1) and (2) may participate in different variants of 4WM. A geometry with two noncollinear pump laser beams is most convenient for studying parametric scattering. 4WM processes described by the phase-matching conditions Eq. (1) or Eq. (2) form scattering cones oriented parallell or perpendicular to the bisector of the pump angle $2\theta_p$ between two pump beams, respectively. The first type of cones results in rings, while the second results in lines on a viewing screen behind the crystal. Equations (1) and (2) allow only 19 independent variants of 4WM processes. All these processes were observed and explained.[22] For a certain time the question of 4WM scattering seemed to be settled in all details. However, new types of parametric scattering were reported recently which could not be explained in the frame of the conventional 4WM model: (1) anomalous light spots in periodically poled $LiNbO_3$:Fe (PPLN)[23,24] and (2) sets of vertical lines in single domain SBN:Cr[25] (see Fig. 1). 4WM models were developed and applied to explain this new parametric scattering. The mixing of coherent optical noise and pump waves was traced to various combinations of noisy gratings either with the domain grating $\mathbf{K}_D$ in PPLN formed by ferroelectric layers with different orientation of the vector $\mathbf{P}_s$, or with the fundamental grating $\mathbf{K}_f=\mathbf{k}_\alpha-\mathbf{k}_\beta$ in SBN recorded by pump beams. It is important to note that in PPLN scattering spots are observed with the vector $\mathbf{K}_D$ parallel to the pump angle bisector, while in SBN the grating vector $\mathbf{K}_f$ is always normal to the bisector. An inclusion of the additional gratings $\mathbf{K}_f$ and $\mathbf{K}_D$ in the phase-matching conditions gives rise for a multitude of new multiwave processes. The unified phase-matching conditions covering all known types of parametric scattering (including those newly reported) were proposed in Ref. 25:

$$\text{rings:}\quad \mathbf{k}_\alpha+\mathbf{k}_\beta+j\mathbf{K}_D=\mathbf{k}_\delta+\mathbf{k}_\gamma, \tag{3}$$

$$\text{lines:}\quad \mathbf{k}_\alpha-\mathbf{k}_\beta+j\mathbf{K}_f=\mathbf{k}_\delta-\mathbf{k}_\gamma, \tag{4}$$

where the index j defines the multiplicity of supplementary phase-matching gratings $\mathbf{K}_f$ or $\mathbf{K}_D$ necessary to fulfill the corresponding phase-matching conditions. For $j=0$, Eqs. (3) and (4) are reduced to Eqs. (1) and (2) of the conventional 4WM model, while for $j\neq 0$ they describe the new scattering processes. Equation (3) perfectly fits vectorial diagrams of the new parametric scattering in PPLN, indicating that anomalous light spots are parts of the scattering cones oriented along the propagation of the pump beams. All scattering lines reported in SBN can be described by Eq. (4) with an even number j. Particular mechanisms resulting in the effective scattering in PPLN are discussed in detail in Ref. 26. The explanation of the new processes of parametric scattering in SBN is only in its initial stages and requires further effort.

In this paper we complete the phenomenological model of new parametric scattering found in SBN[25] and discuss all possible 4WM processes which may result in the scattering. An experimental study of the new 4WM processes is carried out with an example of scattering lines with even indices j observed in a low-doped SBN:Cr crystal. The hysteresis behavior of the new scattering under high external electric fields is reported, showing the strong dependence of the scattering properties on the state of the crystal polar structure. The temperature evolution of the scattering is studied in a wide temperature range covering the transition from the ferroelectric to the paraelectric phase. We show that the temperature of the decay of local polar structures of definite sizes in SBN can be measured by means of parametric scattering and that it depends on the spatial scales of these structures.

II. EXPERIMENTAL SETUP

A single crystal of $Sr_{0.61}Ba_{0.39}Nb_2O_6$ doped with 0.02 wt % Cr_2O_3 was grown by the modified Stepanov technique[27] and cut into cuboids with a thickness of $l=6.1$ mm and a large input face of $a\times c=5.8\times 7.0$ mm^2. The crystal was poled at room temperature by applying an external electric field of $E=6$ kV/cm for 24 h. Afterwards, it was mounted onto a Peltier element in the setup shown in Fig. 1, allowing a temperature adjustment in the range from 10 to 150 °C with an accuracy of 0.01 °C. The crystal was oriented so that the spontaneous polarization $\mathbf{P}_s$ coincides with the Cartesian **z** vector.

The sample was illuminated by two unexpanded beams (α and β in Fig. 1) from either an Ar^+-laser ($\lambda=488$ nm and $d_{FWHM}=1$ mm) or a frequency-doubled Nd-YAG-laser ($\lambda=532$ nm, $d_{FWHM}=1.5$ mm). The beams impinged symmetrically upon the crystal. The pump angle $2\theta_p$ between α and β could be varied between $3°<2\theta_p<180°$. A viewing screen was placed behind the sample to photograph 2D-patterns of light-induced scattering in the y-z plane. To measure the angular intensity distribution $I_s(\theta_s)$ in the scattering pattern along the z axis, a photodetector (not shown in Fig. 1) with an apex angle $\Delta\theta_s=0.5°$ was mounted on a motorized rotation stage at a distance of $L=10$ cm from the sample and was

rotated around it from $-z$ to $+z$ in the angular range of $-90° \leqslant \theta_s \leqslant +90°$ (in air). The scattering angle corresponding to the pump angle bisector was defined as $\theta_s = 0°$. Negative and positive angles correspond to the $-z$ and $+z$ direction, respectively. The angular distribution of the scattering pattern always was measured in the steady state. The entire setup was placed within a black box with only a small hole for the entrance of the pump beam in order to minimize the noise from external light sources.

Both c surfaces of the sample are connected to a dc power supply. The amplitude E_o of the electric field can be varied in the range from -6 kV/cm to $+6$ kV/cm. Fields applied in the direction of the original polarization are considered as positive, while fields applied in the opposite direction are considered as negative. First, the crystal is illuminated homogeneously by incoherent white light to erase any previous holographic gratings. An external field E_o is applied to the illuminated crystal for a duration of 10 s, then it is switched off. After a relaxation time of 1–2 min, the erasing light is turned off and the crystal is illuminated with the pump beams.

III. EXPERIMENTAL OBSERVATION OF NEW PARAMETRIC SCATTERING AND PHENOMENOLOGICAL MODEL

Two coherent extraordinarily polarized beams with the wavelength $\lambda = 488$ nm intersecting in SBN:Cr induce parametric scattering, resulting in series of vertical lines on the viewing screen. The scattering lines have the same polarization as the incident light and are observed only at small pump angles $2\theta_p < 40°$ (measured in air). The number of lines and their angular position strongly depend on the pump angle θ_p. Figure 1 shows the typical scattering pattern observed in SBN:Cr for $\lambda = 488$ nm and pump intensities $I_\alpha = I_\beta = 600$ mW/cm^2. Pump beams are marked by black disks on the viewing screen. At $2\theta_p = 5°$, the pattern consists of three lines in the $-c$ direction and two lines in the $+c$ direction. The line intensity decreases drastically with increasing angle. The parametric scattering appears against the background of beam fanning, with the bright lobe oriented along the $-c$ direction. That results in an additional enhancement of lines on the $-c$ side and a partial depletion of lines on the $+c$ side. The same lines are observed in the backward scattered light propagating towards the incident beams. Similarly to the forward scattering lines, the angular positions of the backward scattering lines depend only on the angle between the pump beams, not on the angle of incidence of the pump beams on the crystal. This indicates that all lines are parts of nested cones with different apex angles and a common axis normal to the pump angle bisector. It is important to note that the lines are not due to a scattering of high orders of diffraction of the pump beams, since there were no such high orders observed in the experiment. If the higher orders of diffraction from the fundamental grating $\mathbf{K}_f$ would exist, they will coincide with scattering lines observed in Fig. 1. The higher diffraction orders may induce the conventional B-process described in Ref. 22 and, respectively, yield the scattering lines at the same angular positions. However, in our particular case, the higher order of diffraction is avoided because of the rather large thickness of the sample. Also, the chosen geometry of the experiment does not allow an effective recording and amplification of the photorefractive gratings via the conventional process described by Eq. (2), because of the zero value of the corresponding electro-optic coefficients r_{13} and r_{23}. The existence of the lines can not be described by any of the phase-matching conditions given by Eqs. (1) and (2) in the frame of the conventional 4WM model of parametric scattering.

We apply a 4WM model based on phase-matching conditions given by Eq. (4) to explain the appearance of lines in Fig. 1 as a result of parametric mixing of the pump waves α and β and two sets of seed waves γj and δj (scattered symmetrically at angles $\pm\theta_s$) on noisy gratings. The noisy gratings are recorded by different pairs of seed and pump waves, and the strong fundamental grating $\mathbf{K}_f = \mathbf{k}_\alpha - \mathbf{k}_\beta$, is recorded only by the pump waves. Pump and seed waves record the following sets of noisy gratings:

$$\mathbf{K}_{sj} = \mathbf{k}_{\gamma j} - \mathbf{k}_\beta, \tag{5}$$

$$\mathbf{K}_{s'j} = \mathbf{k}_\alpha - \mathbf{k}_{\delta j}, \tag{6}$$

$$\mathbf{K}_{dj} = \mathbf{k}_{\delta j} - \mathbf{k}_\beta, \tag{7}$$

$$\mathbf{K}_{pj} = \mathbf{k}_{\gamma j} - \mathbf{k}_\alpha. \tag{8}$$

A general feature of 4WM phase-matching conditions is their invariance to Cartesian coordinates, therefore, a spatial orientation of the wave vectors in Figs. 2, 4, and 5 does not depend on the particular definition of the axes.

Figure 2 shows the phase-matching diagrams for seed-pump pairs α-δj and β-γj for various indices j fulfilled by a combination of the vectors $\mathbf{K}_{sj}$, $\mathbf{K}_{s'j}$ and $j\mathbf{K}_f$. The diagrams are plotted in the plane of the incoming pump beam. The vectors $\mathbf{K}_{sj}$ and $\mathbf{K}_{s'j}$ formed by two symmetric seed-pump pairs are not parallel, but obey the equation

$$\mathbf{K}_{sj} + j\mathbf{K}_f = \mathbf{K}_{s'j} \tag{9}$$

Therefore, diffraction of the wave γj on the combination $(\mathbf{K}_{s'j} - j\mathbf{K}_f)$ and the wave δj on the combination $(\mathbf{K}_{sj} + j\mathbf{K}_f)$ is equivalent to diffraction of these waves on the grating $\mathbf{K}_{sj}$ and $\mathbf{K}_{s'j}$, respectively. This equivalence provides a parametric enhancement of the gratings $\mathbf{K}_{sj}$ and $\mathbf{K}_{s'j}$ and increasing amplitudes of waves γj and δj. After the corresponding substitution of $\mathbf{K}_{sj}$, $\mathbf{K}_{s'j}$ and $\mathbf{K}_f$, Eq. (9) can be rewritten as

$$(j+1)(\mathbf{k}_\alpha - \mathbf{k}_\beta) = \mathbf{k}_{\delta j} - \mathbf{k}_{\gamma j}. \tag{10}$$

Equation (10) is another form of the phase-matching conditions [Eq. (4)] with $\mathbf{K}_f = \mathbf{k}_\alpha - \mathbf{k}_\beta$. According to Eq. (10) and Fig. 2, the larger the index of a line in the series is, the more vectors $\mathbf{K}_f$ are necessary to complete the phase-matching conditions: lines $\gamma 1$ and $\delta 1$ can be formed with a single grating $\mathbf{K}_f$, lines $\gamma 2$ and $\delta 2$ need $2\mathbf{K}_f$, etc. The scattering angle also increases with the index j:

$$\sin\theta_{sj} = (j+1)\sin\theta_p. \tag{11}$$

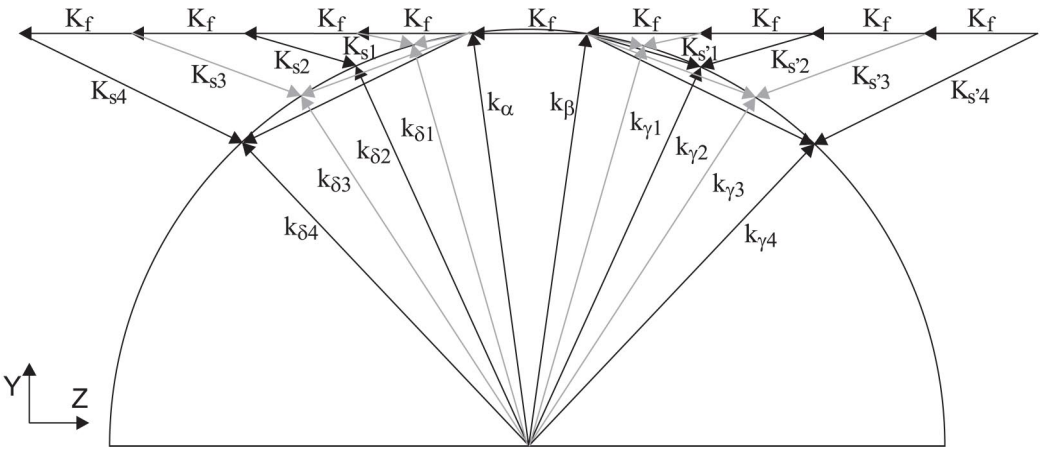

FIG. 2. Phase matching diagrams of 4 WM processes described by Eq. (10): general view in the plane of incidence for $j=1$–4. Lines with odd (even) indices are drawn in grayscale (black), respectively.

The number of lines in a set decreases with increasing pump angle, the largest number of scattering lines, which is possible at a particular pump angle $2\theta_p$, equals $j_{\max}=\text{int}[\sin^{-1}\theta_p-1]$. The theoretical dependence of θ_{sj} on $2\theta_p$ calculated with Eq. (11) is shown in Fig. 3 for the δ-series at $1\leqslant j\leqslant 6$. The angular dependence for the γ-series differs only in the sign of θ_{sj}. The symbols represent the actually observed position of the lines. A comparison of the experimental and theoretical curves shows that only lines with even index j are observed in the experiment. The absence of lines with odd indices indicates that the corresponding 4WM processes are suppressed in SBN. One possible reason for this behavior is that the phases of waves and gratings involved in the process can depend on the parity of the index j. Probably, odd indices result in destructive wave mixing with no effective parametric amplification of seed waves. Below, we will discuss only 4WM processes with even j, while a discussion for odd processes can be performed in a similar way.

We take into account that the grating $\mathbf{K}_f$ considerably extends the possible variants of parametric mixing. Figure 4 shows four 4WM processes with different multiplicity of the supplementary grating $\mathbf{K}_f$ resulting in the same scattering pair $\delta 2$-$\gamma 2$. The diagram *a* is an excerpt from Fig. 2 for $j=2$ showing the mixing via vectors $\mathbf{K}_{sj}$, $\mathbf{K}_{s'j}$ and $2\mathbf{K}_f$ according to Eq. (9). Diagrams *b* and *c* show a mixing via two spatially symmetric sets of vectors $\mathbf{K}_{sj}$, $\mathbf{K}_{dj}$ and $3\mathbf{K}_f$, and $\mathbf{K}_{s'j}$, $\mathbf{K}_{pj}$ and $3\mathbf{K}_f$, respectively:

$$\mathbf{K}_{sj}+(j+1)\mathbf{K}_f=\mathbf{K}_{dj}, \tag{12}$$

$$\mathbf{K}_{pj}+(j+1)\mathbf{K}_f=\mathbf{K}_{s'j}. \tag{13}$$

Finally, diagram *d* is 4WM via a combination of $\mathbf{K}_{pj}$, $\mathbf{K}_{dj}$ and $4\mathbf{K}_f$:

$$\mathbf{K}_{pj}+2j\mathbf{K}_f=\mathbf{K}_{dj}. \tag{14}$$

Parametric amplification of seed waves in the case of Eqs. (12)–(14) is due to the virtual equivalence between different combinations of the noisy gratings $\mathbf{K}_{sj}$, $\mathbf{K}_{s'j}$, $\mathbf{K}_{pj}$, $\mathbf{K}_{dj}$, and the fundamental grating $\mathbf{K}_f$. Corresponding substitutions reduce Eqs. (12)–(14) to the general expression of the phase-matching conditions [Eq. (4)]. Therefore, all of these four 4WM processes should yield the same scattering lines. According to Eq. (11), no even lines should exist at $2\theta_p\gtrsim 39°$, in agreement with the experimental observations. Also, Eq. (11) predicts lines with even index $j=[2$–$20]$ at $2\theta_p=5°$, while only lines with $j=2$, 4, and 6 are found in the experiment. This is because the actual number of lines that can be observed depends on the efficiency of the corresponding 4WM processes, which strongly decreases with the multiplicity of the vector $\mathbf{K}_f$ enclosing the phase-matching diagrams. The efficiency of 4WM processes shown in Fig. 4 decreases from *a* to *d*.

At the same time, the geometry of the new 4WM processes results in additional interesting effects of interference and cascading of 4WM processes, promoting the new parametric scattering. The interference effect is obvious from the fact that different 4WM processes result in the same scattering lines. If parametric processes interfere constructively, the resulting exponential increment describing the total parametric amplification of seed waves should additively increase,[28] and scattering will be considerably enhanced. A cascading effect for scattering waves with even j is shown in Fig. 5(a). The waves $\delta 2$ and $\gamma 2$ are amplified via the primary parametric process given in Fig. 4(a) and can be considered as

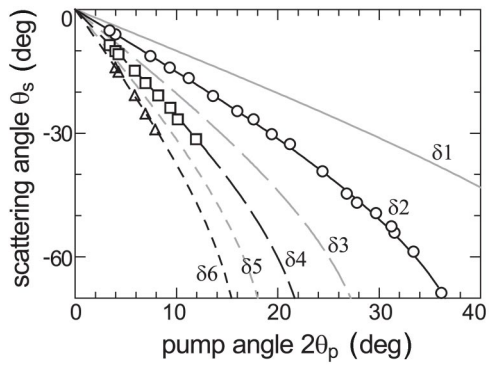

FIG. 3. Scattering angle θ_s vs pump angle θ_p for scattering lines $\delta 1-\delta 6$. Marks are experimental results, while theoretical curves are taken from Eq. (11).

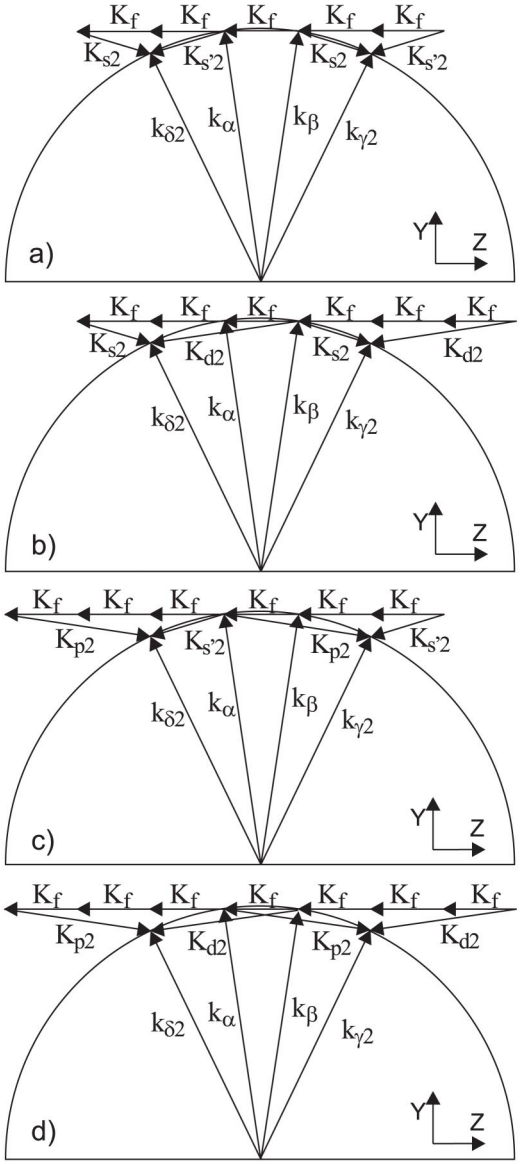

FIG. 4. Phase matching diagrams of 4 WM processes for lines $\delta 2$ and $\gamma 2$ described by Eq. (9) (a), Eq. (12) (b), Eq. (13) (c), and Eq. (14) (d) shown in the plane of incidence.

"pump" waves for the next scattering pair $\delta 4$ and $\gamma 4$, while these waves will serve as the pumps for waves $\delta 6$ and $\gamma 6$, etc. In general case, "pump" waves $k_{\gamma j}$, $k_{\delta j}$ and "scattering" waves $k_{\gamma(j+2)}$, $k_{\delta(j+2)}$ record gratings $\mathbf{K}_{cj}=k_{\delta(j+2)}-k_{\delta j}$ and $\mathbf{K}_{c'j}=k_{\gamma(j+2)}-k_{\gamma j}$, which difference is always $\mathbf{K}_{cj}-\mathbf{K}_{c'j}=\mathbf{K}_{s2}-\mathbf{K}_{s'2}=2\mathbf{K}_f$. Therefore, the pump energy can be effectively transferred to waves with larger index via waves with smaller j. At the same time, the cascading effect for odd j is expected to be less effective, because the relation $\mathbf{K}_{cj}-\mathbf{K}_{c'j}=\mathbf{K}_{s1}-\mathbf{K}_{s'1}$ is not fulfilled. As it is shown in Fig. 5(b), $\mathbf{K}_{cj}-\mathbf{K}_{c'j}=2\mathbf{K}_f$, while $\mathbf{K}_{s1}-\mathbf{K}_{s'1}=\mathbf{K}_f$.

According to the conventional model of the photorefractive effect,[8] recording of refractive index gratings in SBN:Cr occurs as follows: An interference pattern formed by two coherent waves excites electrons into the conducting band from donor levels Cr^{3+} in regions of high light intensity. The

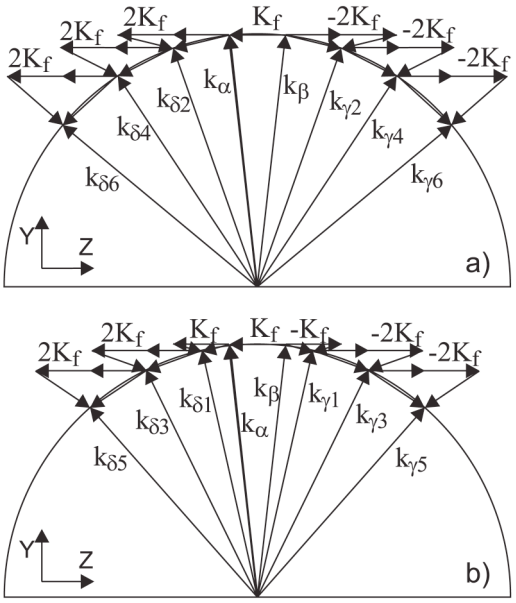

FIG. 5. Phase matching diagrams depicting a cascading effect in parametric multiwave mixing.

electrons migrate due to thermal diffusion and are trapped by acceptor levels Cr^{4+} in regions of low light intensity. The resulting space-charge field modulates the index of refraction via the linear electro-optic effect, and a photorefractive grating is recorded. The 4WM efficiency depends on the strength of the recorded gratings, particularly on the strength of the fundamental grating $\mathbf{K}_f$. The grating strength in turn depends on the contrast of the interference pattern and on the pump angle between α and β. Therefore, the scattering intensity exhibits a strong dependence on the pump ratio $m_p=I_\alpha/I_\beta$[25] and on the angle θ_p. Figure 6 shows the dependence of the scattering intensity of the lines $\delta 2$ and $\delta 4$ on the pump angle. The intensity of both lines is measured in the plane of incidence and then normalized with the pump intensity $I_p^\Sigma=I_\alpha+I_\beta$. The decrease of the scattering intensity of line $\delta 2$ observed at $2\theta_p>20°$ is due to the space-charge limitation at the increasing spatial frequency, which is typical for SBN. For comparison, the two-beam coupling coefficient measured as $\Gamma l=\frac{1}{2}\ln[I_\alpha(l)I_\beta(0)/I_\alpha(0)I_\beta(l)]$ is also shown in Fig. 6. The drop of the intensity of line $\delta 4$ occurs at smaller angles than of line $\delta 2$ because $\mathbf{K}_{s'4}$, $\mathbf{K}_{p4}$, $\mathbf{K}_{d4}>\mathbf{K}_{s'2}$, $\mathbf{K}_{p2}$, $\mathbf{K}_{d2}$. The de-

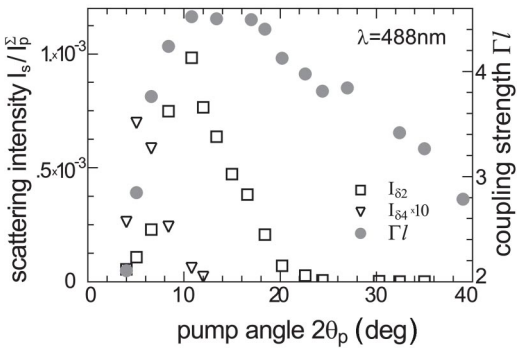

FIG. 6. Dependence of the intensity of lines $\delta 2$ and $\delta 4$ and two-beam coupling coefficient Γl vs the pump angle $2\theta_p$.

crease of the scattering intensity at small angles is a clear indication of the photorefractive origin of the new scattering: the diffusion process dominating the charge transport in SBN is a sine function of the angle between two waves at small recording angles. Note that gratings recorded in materials with dominating diffusion are $\pi/2$-shifted with respect to the initial interference patterns. Such a spatial shift allows an additional light amplification by two-wave coupling in the $-c$ direction, which usually leads to the development of spatially asymmetric beam fanning[10] seen in Fig. 1. Direct pump-seed coupling also results in an additional enhancement of the lines in the $-c$ direction and a depletion in the $+c$ direction.

A presence of scattering lines with even j and an absence of ones with odd j cannot be explained by considering only the phase-matching diagrams. An appearance of the particular type of parametric scattering is defined by the efficiency of the corresponding 4WM process, which in its turn depends on photorefractive properties of the medium. For instance, as it is shown for ring-scattering processes fulfilled via the domain grating $\mathbf{K}_D$ oriented in the direction of wave propagation, the processes with even j are only effective via a photovoltaic contribution to the photorefractive recording, while diffusion governs processes with odd j.[26] It is because of different properties of the photovoltaic and diffusion response in the periodically poled structures. However, such a trend is not the case for a homogeneously poled SBN and line-scattering processes fulfilled via the fundamental grating $\mathbf{K}_f$ orthogonal to the pump angle bisector. Here, the effect of the photovoltaic and diffusion contribution on the efficiency of even and odd parametric processes should be different from that reported for PPLN. An intricate and multicompound configurations of 4WM greatly complicates a theoretical analysis of the parametric amplification processes. A derivation of the exact expression of the corresponding amplification coefficients requires an elaboration of a new 4WM theory adapted to the new phase-matching conditions, which is beyond of the scope of this paper.

IV. FERROELECTRICITY DRIVEN PROPERTIES OF PARAMETRIC SCATTERING

SBN is a typical relaxor ferroelectric, which means that the polar structure does not immediately break down at a sharp phase transition temperature; instead, local polar clusters survive far into the paraelectric phase. Usually, the temperature T_m of the maximum of the dielectric response is taken as the transition temperature. However, the value thus received is an integrated response of the crystal over different domain/cluster sizes. Because of the strong temperature dispersion of the decay of different scales in the polar structure,[17] a phase transition temperature cannot be defined and measured.

For doped SBN, T_m is rather close to the room temperature. In the ferroelectric phase, the polar structure of SBN consists of ferroelectric domains of different sizes from dozens of nanometers to hundreds of micrometers.[29] Electric poling of the sample aligns most of the domains along the direction of the external field, yielding a non-zero polarization in the crystal. However, poling does not eliminate bulk domains completely. For temperatures higher than the phase transition temperature, the domain structure is substituted by less stable polar clusters causing nonzero macroscopic polarization, decaying gradually with temperature. As the linear electro-optic effect is a function of the spontaneous polarization P_s, the efficiency of photorefractive recording in SBN depends on the state of the polar structure. The largest electro-optic coefficient r_{33}, which is mainly responsible for the gratings shown in Figs. 2, 4, and 5 can be written as:[30]

$$r_{33} = 2g_{33}P_3\varepsilon_{33}\varepsilon_o, \tag{15}$$

where $P_3 = P_s$, g_{33} is the quadratic electro-optic coefficient, and ε_{33} and ε_o are dielectric permittivity and dielectric constant. Any changes in the polar state will affect light-induced scattering. The appearance and efficiency of the scattering can be controlled by external electric fields via $\mathbf{P}_s$. In an electrically poled sample with most domains oriented in one direction, the photorefractive response and light-induced scattering are very pronounced. However, at a negative external field E_o equal to the coercive field E_c, the spontaneous polarization and electro-optic coefficient approach zero, and all photorefractive properties vanish. Intensity and angular distribution of the seed scattering is also defined by the spatial order of the ferroelectric domains in SBN. According to the model of seed scattering,[17] photorefractive scattering centers in SBN are anomalies of the refractive index δn induced via the linear electro-optic effect by internal electric fields located on domain tips. In an electrically poled sample with spatially ordered ferroelectric domains, δn-anomalies form diffraction structures with different spatial frequencies defined by the size Λ of the corresponding domains. Diffraction of the incident light on δn-structures with the spatial period Λ results in seed scattering propagating at the angle $\theta_s = 2\arcsin(\lambda/2\Lambda)$. Seed scattering propagating at small θ_s corresponds to large domains, while large-angle scattering is due to small domains. The efficiency of the seed scattering increases in samples with a well-ordered polar structure (poled samples) and decreases in samples with a disordered structure (unpoled samples).[15] Since the spontaneous polarization and the polar structure decay when the crystal is heated above T_m, light-induced scattering decreases as well. For different spatial scales this decrease occurs at different temperatures, since smaller domains are less stable than larger ones. This makes parametric scattering a particularly interesting tool for a contactless study of the relaxor phase transition. The parametric scattering observed in SBN has angle-selective properties: 4WM results in the enhancement of scattering components propagating only in the angular interval defined by the corresponding phase-matching conditions. The recorded photorefractive gratings correspond to the limited spectrum of spatial frequencies in the polar structure. Therefore, the temperature evolution of the parametric scattering should possess all necessary information on the temperature dependent decay of the polar structure with the particular spatial scale. Note that the angular-selective nature is an important advantage of the parametric scattering compared to beam fanning, when the task is to study the particular spatial scale in the polar structure of the crystal. With beam fanning one can evaluate the state of the polar structure

in a rather wide spatial spectral range, while we restrict the analysis only to domains with the certain size Λ defined by the scattering angle θ_s due to parametric scattering. These two methods may complete each other when applied to the study of changes in the polar structure caused by external fields or by thermal heating. The corresponding results received by the beam fanning method are represented in Refs. 15–17. Below we apply the new parametric scattering to analyze some particular polar scales (1) at the spatial reversal and the ferroelectric hysteresis, and (2) at the thermal decay over the phase transition.

A. Spatial reversal and hysteresis behavior of parametric scattering

To study the spatial reversal of the domain structure, first a high external field $E_o=-5.0$ kV/cm is applied to the SBN sample at room temperature. After the field is switched off and the crystal is illuminated by the two pump beams with the wavelength $\lambda=488$ nm and intensities $I_\alpha=I_\beta=600$ mW/cm^2, the scattering pattern on the viewing screen appears spatially reversed compared to the pattern shown in Fig. 1: Now the strong lines develop at positive angles and weak lines at negative angles. The total scattering intensity is almost unchanged by the repoling procedure. The lobe of beam fanning also switches its orientation to positive angles θ_s. All these changes are due to the spatial reversal of $\mathbf{P}_s$ by the negative external field. The absolute value of $\mathbf{P}_s$ was not changed by this procedure, since the total amount of the scattered light was the same before and after the reversal. The $\mathbf{P}_s$ reversal does not affect the efficiency of the 4WM processes, but inverses the direction of the two-wave coupling. Posterior application of a positive electric field $E_o=5.0$ kV/cm switches the vector $\mathbf{P}_s$ and the scattering pattern back to its original state.

The evolution of the parametric scattering pattern under a gradually increasing external field allows to study the ferroelectric hysteresis. A pump angle $2\theta_p=28°$ is chosen so that only two lines $\delta 2$ and $\gamma 2$ appear in the scattering pattern (see Fig. 2). E_o is changed in small steps from zero to $E_o=-5$ kV/cm, then increased in the opposite direction to $E_o=5$ kV/cm. After the reduction of the field back to $E_o=0$ the hysteresis loop is closed. After each step, the value of the scattering ratio coefficient $m_s=(I_{\delta 2}-I_{\gamma 2})/(I_{\delta 2}+I_{\gamma 2})$ is determined as a measure of the spatial order in the polar structure. This coefficient depends on the state of spontaneous polarization in the crystal and changes its sign when the scattering pattern and $\mathbf{P}_s$ are reversed by the external field. Two complete loops of the ferroelectric hysteresis were performed. Figure 7 shows the corresponding dependence of m_s on E_o. The horizontal plateau on the scattering hysteresis curves correspond to the two stable states of the polar structure with mutually opposite orientations of $\mathbf{P}_s$. The end point of the second loop is marginally lower than that of the first loop, implying a gradual reduction of the spontaneous polarization during repoling at room temperatures. The scattering ratio m_s passes through zero when the external field E_o approaches the coercive field E_c. The coercive field is asymmetric for both loops: On the negative side, it remains constant at $E_c=-2.4$ kV/cm for both hysteresis loops, but on the positive side it increases from $E_c=2.75$ kV/cm for the first loop to $E_c=4.4$ kV/cm for the second loop. This difference can be explained by the pinning effect usually observed in ferroelectric hysteresis experiments.[31] At the same time, further repetitions of the experiment show rather good reproducibility of the scattering hysteresis: the next two loops are almost the same as the second loop. This can be attributed to the minimization effect of optical irradiation on the domain pinning earlier reported for highly doped SBN.[15,32]

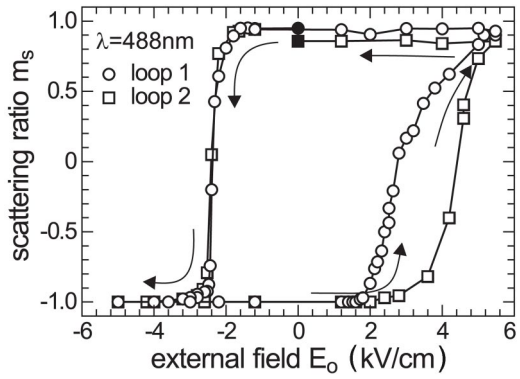

FIG. 7. Scattering hysteresis measured at $\lambda=488$ nm: coefficient m_s vs external electric field E_o. First and second loops are marked by circles and squares, respectively. The solid symbols label the start and the end points of the first and second loop, respectively. The arrows show the direction of the change of E_0.

In conclusion, the observation of the scattering hysteresis proves that the photorefractive response in SBN is a function of the polar structure of the crystal and can be applied to the study of its ferroelectric properties.

B. Temperature evolution of parametric scattering

The temperature study of the parametric scattering was performed at a pump beam wavelength of $\lambda=532$ nm and intensities of $I_\alpha=I_\beta=300$ mW/cm^2. The photorefractive response in SBN decreases with increasing wavelength. At the chosen wavelength only two lines $\delta 2$ and $\gamma 2$ are observed over the whole pump angle interval, and therefore no influence to the temperature dependence of these lines from other lines is expected. The vectors $\mathbf{K}_f$, $\mathbf{K}_{s2}$ and $\mathbf{K}_{s'2}$ involved in the corresponding 4WM processes have nearly the same spatial periods. The temperature evolution of light-induced scattering was measured at two different pump angles $2\theta_p=3.4°$ and 12° corresponding to one of the lowest and the highest intensity of the line $\delta 2$, respectively. The first angle corresponds to spatial structures with a period $\Lambda=9$ μm, while the second one selects $\Lambda=2.5$ μm. Figure 8 shows angular profiles of the light intensity behind the sample measured for three different temperatures $T=25$, 63, and 90 °C. All scans present steady state intensity distributions in the plane of incidence. The two central maxima are caused by the transmitted pump beams, while two peaks appearing at larger angles are scattering lines. The complete temperature dependence of the total intensity of the parametric scattering $I_s^\Sigma=I_{\delta 2}+I_{\gamma 2}$ measured at $2\theta_p=12°$ and 3.4 ° is shown in Figs.

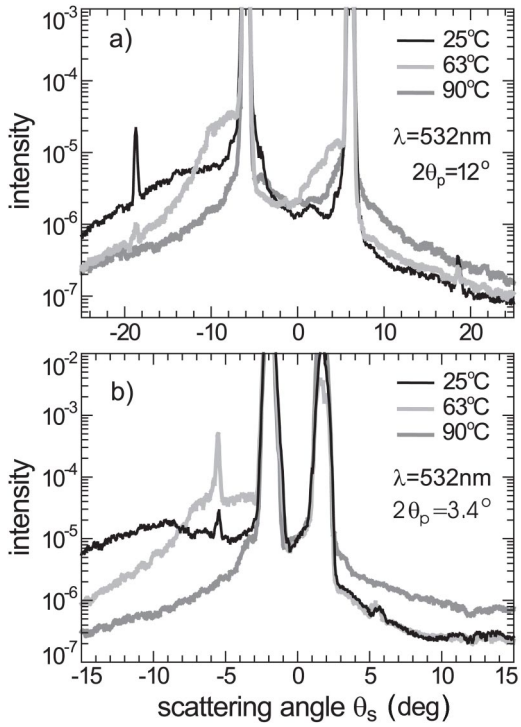

FIG. 8. Angular profiles of scattering pattern in the plane of incidence measured at $T=25$, 63, and 90 °C for $2\theta_p=12°$ (a) and 3.4° (b).

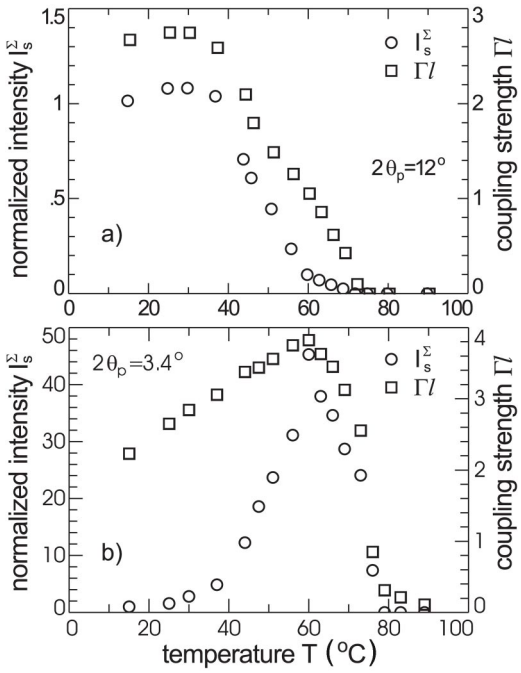

FIG. 9. Temperature dependence of scattering intensity I_s^Σ and two-beam coupling coefficient Γl measured at $2\theta_p=12°$ (a) and 3.4° (b).

9(a) and 9(b), respectively. The curves are normalized to I_s^Σ at $T=15$ °C, marked by circles. At $2\theta_p=12°$, the lines remain almost unchanged in intensity at low temperatures, decrease at $T>30$ °C, and vanish at $T=72$ °C. A different behavior is observed at $2\theta_p=3.4°$: First, the line intensity strongly increases with increasing temperature, peaks at $T=60$ °C and vanishes to zero at $T=79$ °C. A qualitatively similar temperature behavior is observed for two-beam coupling under comparable geometrical conditions. The corresponding curves of the coupling coefficient Γl are shown in Figs. 9(a) and 9(b) by squares. These results can be interpreted in light of the fact that scattering components propagating at different angles are associated with different domain structures. The photorefractive response in SBN depends on the electro-optic coefficient r_{33}, which increases with temperature.[6] This is the reason of the strong increase of scattering lines at small pump angles. At the same time, the spatial disorder and the following decay of the domain structure occurring above T_m weaken the photorefractive grating recording. Note again that because of the relaxor behavior the spontaneous polarization and photorefractive properties of SBN do not vanish abruptly, but decay gradually with temperature. Since small-scale structures decay faster and easier than large-scale structures, the decrease of the parametric scattering at large angles takes place at lower temperatures than for small angles. The maximum of I_s at a particular angle θ_s indicates the decay temperature of polar structures with the particular size $\Lambda = \lambda/2 \sin \theta_s/2$. Since conventional phase transition measurement methods always average over domains of all sizes, they result in much higher values of T_m.

V. CONCLUSION

A complete phenomenological analysis of new processes of parametric light-induced scattering recently found in SBN has been presented. The conical scattering induced by two pump beams and resulting in series of light lines is caused by 4WM processes between scattering and pump waves involving the fundamental grating recorded by the pump beams. Generalized phase-matching conditions for the new 4WM processes are derived. The properties of the scattering have been investigated in low-doped SBN:Cr at different temperatures and under externally applied electric fields. Parametric scattering is suggested as a promising tool giving an additional information on ferroelectric and relaxor properties of SBN at the certain domain size selected by the corresponding phase matching conditions. The scattering hysteresis has been found and interpreted as the result of a strong correlation between the photorefractive and ferroelectric properties of SBN. The decay of polar areas of different spatial scale above the relaxor phase transition has been observed directly from the temperature dependence of the scattering intensity. The study of the new scattering is of paramount importance for further developments of the 4WM theory and for a better understanding of processes of parametric amplification of coherent noise in nonlinear optical materials.

ACKNOWLEDGMENT

This work is supported by INTAS (Project 01-0173), DFG (Wo618/3-4, GRK695).

*Present address: Institute of Materials Science, Darmstadt University of Technology, Germany.
[1] J. Neumann, S. Mendricks, E. Krätzig, M. Goul'kov, and S. Odoulov, Opt. Commun. **146**, 220 (1998).
[2] S. Breugnot, H. Rajbenbach, M. Defour, and J.-P. Huignard, Opt. Lett. **20**, 1568 (1995).
[3] D. Dolfi, A. Delbouble, and J.-P. Huignard, Electron. Lett. **29**, 450 (1993).
[4] R. A. Rupp, J. Seglins, and U. van Olfen, Phys. Status Solidi A **168**, 445 (1991).
[5] M. Fally, M. A. Ellabban, R. A. Rupp, M. Fink, and J. Wolfsberger, Phys. Rev. B **61**, 15778 (2000).
[6] M. Goulkov, T. Granzow, U. Dörfler, Th. Woike, M. Imlau, R. Pankrath, and W. Kleemann, Opt. Commun. **218**, 173 (2003).
[7] M. Goulkov, M. Imlau, R. Pankrath, T. Granzow, U. Dörfler, and Th. Woike, J. Opt. Soc. Am. B **20**, 307 (2003).
[8] N. V. Kukhtarev, V. P. Markov, S. G. Odoulkov, M. S. Soskin, and V. L. Vinetskii, Ferroelectrics **22**, 961 (1979).
[9] P. Yeh, *Introduction to Photorefractive Nonlinear Optics* (John Wiley, New York 1993).
[10] V. V. Voronov, I. R. Dorosh, Yu. S. Kuz'minov, and N. V. Tkachenko, Sov. J. Quantum Electron. **10**, 1346 (1980).
[11] J. Feinberg, J. Opt. Soc. Am. **72**, 46 (1982).
[12] M. Goulkov, S. Odoulov, Th. Woike, M. Imlau, and H. Hesse, Phys. Rev. B **65**, 195111 (2002).
[13] R. Magnusson, and T. K. Gaylord, Appl. Opt. **13**, 1545 (1974).
[14] S. G. Odoulov, B. I. Sturman, and M. Yu. Goul'kov, J. Opt. Soc. Am. B **13**, 577 (1996).
[15] M. Goulkov, T. Granzow, U. Dörfler, T. Woike, M. Imlau, and R. Pankrath, Appl. Phys. B: Lasers Opt. **76**, 457 (2003).
[16] M. Goulkov, M. Imlau, T. Granzow, and Th. Woike, J. Appl. Phys. **94**, 4763 (2003).
[17] M. Goulkov, O. Shinkarenko, T. Granzow, M. Imlau, and Th. Woike, Europhys. Lett. **66**, 48 (2004).
[18] M. Imlau, R. Schieder, R. A. Rupp, and Th. Woike, Appl. Phys. Lett. **75**, 16 (1999).
[19] E. K. Kirilenko, Sov. J. Quantum Electron. **19**, 930 (1989).
[20] T. M. Smirnova and E. A. Tikhonov, Sov. J. Quantum Electron. **9**, 93 (1979).
[21] I. C. Khoo and Y. Liang, Phys. Rev. E **62**, 6722 (2000).
[22] B. I. Sturman, S. G. Odoulov, and M. Yu. Goulkov, Phys. Rep. **275**, 197 (1996).
[23] B. I. Sturman, M. Aguilar, F. Agulló-López, V. Pruneri, P. G. Kazansky, and D. C. Hanna, Appl. Phys. Lett. **69**, 1349 (1997).
[24] M. Goul'kov, S. Odoulov, I. Naumova, F. Agulló-López, G. Calvo, E. Podivilov, B. Sturman, and V. Pruneri, Phys. Rev. Lett. **86**, 4021 (2001).
[25] M. Goulkov, O. Shinkarenko, L. Ivleva, P. Lykov, T. Granzow, Th. Woike, M. Imlau, and M. Wöhlecke, Phys. Rev. Lett. **91**, 243903 (2003).
[26] E. Podivilov, B. Sturman, M. Goul'kov, S. Odoulov, G. Calvo, F. Agulló-López, and M. Carrascosa, J. Opt. Soc. Am. B **19**, 1582 (2002).
[27] L. I. Ivleva, N. V. Bogodaev, N. M. Polozkov, and V. V. Osiko, Opt. Mater. (Amsterdam, Neth.) **4**, 168 (1995).
[28] M. Yu. Goul'kov, S. G. Odoulov, B. I. Sturman, A. I. Chernykh, E. Krätzig, and G. Jakel, J. Opt. Soc. Am. B **13**, 2602 (1996).
[29] G. Fogarty, B. Steiner, M. Cronin-Golomb, U. Laor, M. H. Garrett, J. Martin, and R. Uhrin, J. Opt. Soc. Am. B **13**, 2636 (1996).
[30] J. R. Oliver, R. R. Neurgaonkar, and L. E. Cross, J. Appl. Phys. **64**, 37 (1988).
[31] T. Granzow, U. Dörfler, Th. Woike, M. Wöhlecke, R. Pankrath, M. Imlau, and W. Kleemann, Phys. Rev. B **63**, 174101 (2001).
[32] U. Dörfler, T. Granzow, Th. Woike, M. Wöhlecke, R. Pankrath, and M. Imlau, Appl. Phys. B: Lasers Opt. **78**, 211 (2004).